6-8-2020

Aerodynamic and Aeroacoustic Performance of Small UAV Propellers in Static Conditions

William Jordan
North Carolina State University

Robert W. Deters
Embry-Riddle Aeronautical University, DETERSR1@erau.edu

Shreyas Narsipur
North Carolina State University

Aerodynamic and Aeroacoustic Performance of Small UAV Propellers in Static Conditions

William Jordan*, Shreyas Narsipur†
Dept. of Mechanical and Aerospace Engineering,
North Carolina State University, Raleigh, NC 27695-7910

Robert W. Deters‡
Dept. of Engineering and Technology,
Embry-Riddle Aeronautical University - Worldwide, Daytona Beach, FL 32114

The proliferation of small multi-rotor UAVs in commercial, recreational, and surveillance spheres has garnered significant interest in the noise produced by these vehicles. The current research aims to study the relationship between the aerodynamic performance and acoustic characteristics of small-scale UAV propellers. Three commercially available propellers for the DJI Phantom 2/3 UAV were selected for preliminary development and validation of an aeroacoustic experimental test setup and associated data reduction methods. Propeller thrust, torque, and power measurements were recorded at static conditions. Upon successful validation of the test bench, acoustic measurements were taken at the propeller disk's upstream and in-plane locations. The power spectral density of these acoustic signals was estimated using the modified periodogram (Welch's) method to identify frequency content and calculate sound pressure levels (SPLs) at each of the observation locations. Additionally, time-frequency analysis verified the periodogram results and identified possible sources of transient noise at static thrust. These methods found the nonrotor noise to be a major contributor to the SPL at higher frequencies and the propeller noise dominating the SPL spectra at the lower frequencies. Experimental thrust, torque, power, and sound pressure level (SPL) data were then compared for each propeller to identify relationships between aerodynamic performance and acoustic characteristics with variations in propeller geometry and blade loading.

BPF	=	blade passing frequency (Hz)
C_P	=	power coefficient
C_Q	=	torque coefficient
C_T	=	thrust coefficient
E	=	power spectra (W/Hz)
f	=	frequency (Hz)
f^+	=	non-dimensional frequency
f_s	=	sampling frequency (Hz)
δf	=	frequency resolution (Hz)
G	=	pre-multiplied spectra magnitude
$OASPL$	=	Overall Sound Pressure Level (dB)
P	=	propeller power (W)
p_{ref}	=	reference pressure: 20 $\mu Pa/\sqrt{Hz}$
PSD	=	power spectral density (W/Hz)
Q	=	propeller torque (N-m)
Re	=	Reynolds Number
SPL	=	Sound Pressure Level (dB)
T	=	propeller thrust (lb, N)
V	=	flow velocity (m/s)

*Undergraduate Student, wajordan@ncsu.edu
†Teaching Assistant Professor, shreya@ncsu.edu. Member AIAA
‡Assistant Professor, detersr1@erau.edu. Member AIAA

ρ	=	density (kg/m^3)
μ	=	dynamic viscosity ($N\text{-}s/m^2$)
θ	=	sensor angular location relative to propeller disk plane (degrees)
ω	=	angular frequency (rad/s)
$\psi(t)$	=	wavelet function
$\Psi(\omega)$	=	wavelet function in frequency domain

I. Introduction

The popularity of using small unmanned aerial vehicles (UAVs) for recreational, commercial, and research activities has increased the need for performance data for these aircraft. On the commercial side, it is likely that small UAVs may soon be delivering packages in areas of higher populations. As flights of small UAVs near people become more common, aircraft noise and its effect on people must be considered [1]. The multirotor design is common with small UAVs due to its vertical takeoff and landing capability. With a multirotor, the propellers are the source of lift so the performance characteristics (thrust and power) are important for efficient designs. The propellers are also the main source of noise with multirotors. Designs of new multirotors that fly near people will need to be optimized for thrust, power consumption, and noise.

Thrust and power data for a variety of small-scale propellers are available [2–8]. The main conclusion from performance tests on these small-scale propellers is that they are not as efficient as their full-scale counterparts. The reason for the lower efficiency is due to the low Reynolds numbers in which they operate. Propellers with diameters of 9 in. and smaller have Reynolds numbers less than 100,000. In addition to performance measurements, acoustic tests of a few propellers have been done. Some tests measured the noise of a few off-the shelf propellers, though most focused on the noise produced from a few custom propellers [9–13]. Tests with larger data sets have focused on off-the-shelf 16-in. propellers [14] or custom propellers using the NACA 0010 airfoil [15]. There are little data on the many available off-the-shelf propellers with diameters around 9 in. with their corresponding performance results.

The purpose of this study is to measure and compare the acoustic behavior of three off-the-shelf propellers used on the popular DJI Phantom. Each propeller is tested at multiple rotational speeds at static conditions. Aerodynamic performance of these propellers were tested prior by the authors [3]. The results of this study provide a baseline database of propeller performance and aeroacoustics.

II. Methodology

A. Aerodynamic Data Collection and Processing

1. Equipment

Static performance results of the propellers were gathered previously using the University of Illinois at Urbana-Champaign's propeller thrust and torque balance [3]. Figure 1 provides a drawing of the balance. Thrust was measured using the T-shaped pendulum balance that pivoted about two flexural pivots and was constrained on one side by a load cell [16]. An Interface SM S-Type load cell with a load capacity of 25 lb (111 N) was used for these tests. The balance was designed to allow the load cell to be placed in ten different locations to use the full range of the load cell based on the thrust produced. The load cell locations ranged from 3.25 in. (8.26 cm) from the pivot point to 7.75 in. (19.69 cm) in 0.5-in. (1.27-cm) increments.

The torque from the propeller was measured using a reaction torque sensor (RTS) from Transducer Techniques. A 100 oz-in. (0.706 N-m) transducer was used. To remove as much of the testing rig from the propeller slipstream as possible, a fairing was used to surround the motor sting, balance support arm, and wires. Additional details about the balance and fairing can be found in Deters, et al. [2, 17]

A red laser and phototransistor were used to measure the propeller RPM. As the propeller spins, the propeller blades block the laser and cause the voltage read from the phototransistor to drop near zero. The peaks from the resulting square wave were counted over a sample time to determine the RPM. Specifications about the RPM measurement system are available in Deters et al. [2, 17]

To provide power to the motors, a BK Precision 1688B power supply was used. The ambient pressure was measured using a Setra Model 270 pressure transducer, and the ambient temperature was measured using a digital thermometer.

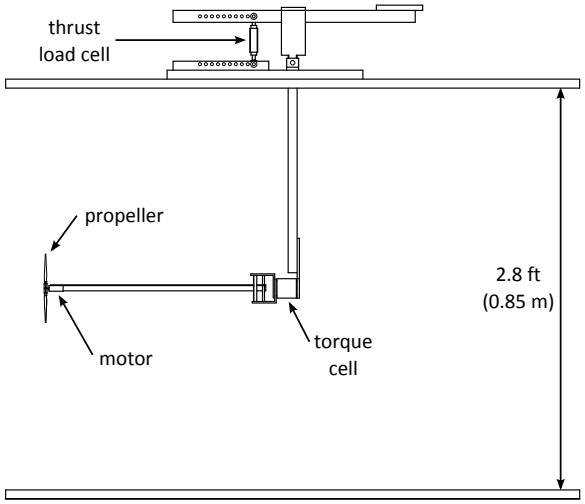

Fig. 1 Propeller thrust and torque balance.

2. Testing Procedure

During a static performance test, the thrust, torque, input voltage, and input current were measured over a range of RPMs. A LabVIEW® program was written to automatically set the propeller RPM and record the resulting performance data. To control the RPM, a personal computer commanded a voltage to a modified ServoXciter EF from Vexa Control using a National Instruments PCI-6031E 16-bit analog-to-digital data acquisition (DAQ) board. The ServoXciter then sent a signal to the electronic speed controller to rotate the motor. Once the desired RPM value was reached, the thrust and torque data were recorded by the DAQ board. Simultaneously with the thrust and torque measurements, the ambient pressure was also measured. To fully capture the RPM, the voltages from the phototransistor were recorded at a higher rate than the rest of the measurements. The propeller RPM was measured first followed by the measurement of the thrust and torque.

3. Data Reduction

Using the measured ambient pressure and temperature, the air density was calculated from the equation of state

$$p = \rho RT \tag{1}$$

where R is the universal gas constant. The standard value of 1716 $\text{ft}^2/\text{s}^2/^\circ\text{R}$ (287.0 $\text{m}^2/\text{s}^2/\text{K}$) for air was used.

Propeller power is calculated from the measured propeller torque by

$$P = 2\pi nQ \tag{2}$$

Performance of a propeller is typically given in terms of the thrust, torque, and power coefficients, defined as

$$C_T = \frac{T}{\rho n^2 D^4} \tag{3}$$

$$C_Q = \frac{Q}{\rho n^2 D^5} \tag{4}$$

$$C_P = \frac{P}{\rho n^3 D^5} \tag{5}$$

where nD can be considered the reference velocity and D^2 can be considered the reference area.

The Reynolds number of the propeller is calculated based on the rotational speed and chord at the 75% blade station. The Reynolds number is defined as

$$Re = \frac{\rho V c}{\mu} \tag{6}$$

where the viscosity μ was calculated from Sutherland's formula.

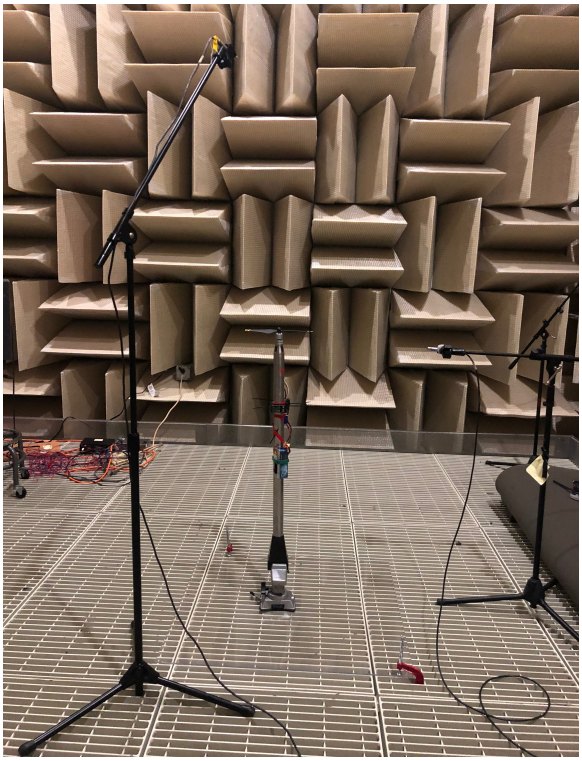

Fig. 2 Experimental setup in the anechoic chamber.

B. Acoustic Data Collection and Processing

1. Equipment

Acoustic data was collected at the NC State University anechoic chamber. The chamber has interior dimensions of 17 ft deep by 17 ft wide by 17.4 ft high. The chamber possesses a low frequency cut off at approximately 80 Hz and meets the qualification requirements for an anechoic chamber given in ISO 3745. A metal grate floor provides a surface to walk on, and was used to fix the experimental setup in place. The experimental setup in the anechoic chamber is shown in Fig. 2.

SPL data was recorded by a National Instruments PXI-4462 Sound and Vibration Module connected to 2 Bruel & Kjaer Type 4188-A-021 microphones. One microphone was positioned in-plane with the propeller disk approximately 23 in. (0.58 m) from the motor shaft. The other microphone was positioned approximately 39 in. (1.0 m) above and upstream of the propeller disk. This arrangement is shown in Fig. 3.

A DJI 2312 brushless DC (BLDC) motor was paired with a Castle Creations Phoenix Edge 50 Amp ESC to drive the propellers. The DJI 2312 is a 14-pole, 12 slot outrunner motor with motor velocity constant 960 kv. Throttle control for the ESC was provided via PWM input from a Flysky FS-iA6B receiver. The motor was mounted to a 1 meter long aluminum sting via a 3D-printed adaptor mount. The sting was attached to a vice clamp, which was in turn attached to a fixed plexiglass plate via a suction mount. The ESC, radio receiver, and wiring were fastened to the side of the aluminum sting with hook and loop fasteners. Care was taken to isolate rigid components from direct contact with the aluminum sting, so as to reduce structural noise. The ESC was powered by a 22,000 mAh 6S LiPo battery pack and power consumption was monitored using a Medusa Research Power Analyzer Pro system. These components were located at the base of the sting. The aeroacoustic test bench setup in the anechoic chamber, consisting of the sting assembly (containing the motor, propeller, ESC, and receiver) and the microphones, is shown in Fig. 2.

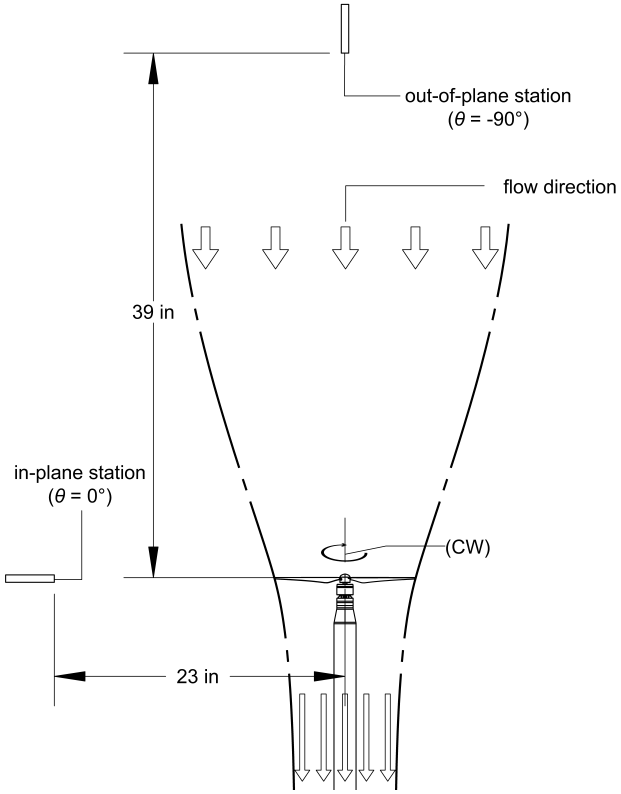

Fig. 3 Microphone location and orientation.

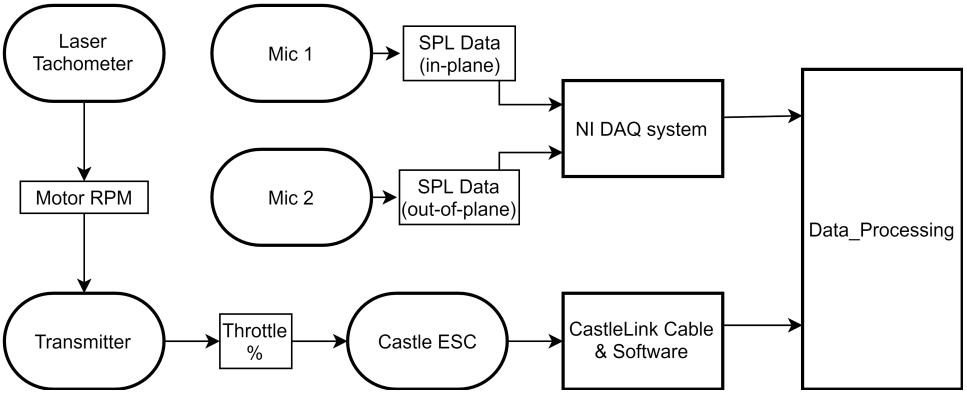

Fig. 4 Aeroacoustic data acquisition methodology.

2. Testing Procedure

Propeller rotation speed was approximated from a handheld laser tachometer and adjusted to the target RPM using radio transmitter throttle input. The SPL was recorded by the two microphones at 48 kHz for a nominal duration of 10 s. Not all tests recorded the full duration of 10 s, so all audio files were trimmed to have the same signal length to keep the number of samples constant. The trimmed audio data for each test had a duration of 4.792 s, corresponding to 230,000 samples.

Due to the imprecise RPM measurement afforded by the handheld tachometer, logged RPM data was downloaded from the ESC via a Castle Link USB adapter cable after each recorded test. RPM data from the last 10 s of continuous operation was then time averaged to provide the estimated mean motor RPM. The data collection methodology is summarized in Fig. 4.

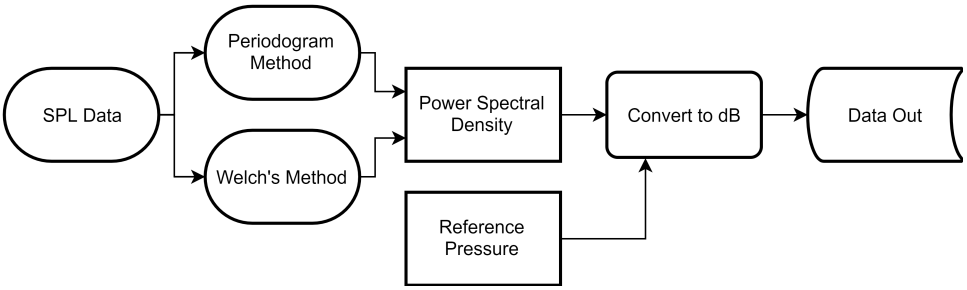

Fig. 5 Aeroacoustic data post-processing methodology.

3. Data Reduction

Data processing was conducted in MATLAB® using built-in functions for calculating power spectral density estimates. The MATLAB® `periodogram()` function was employed using the default periodogram method and Welch's method. Both methods were explored for data post-processing. The procedure for post-processing data is summarized in Fig. 5. The single sided periodogram is an estimate of power spectral density (PSD) of a real-valued signal x_n [18]. The single sided periodogram at sensor location θ_j is given as:

$$PSD\left(\theta_j, f\right) = 2\frac{\Delta t}{N}\left|\sum_{n=0}^{N-1} x_n e^{-j2\pi f \Delta t n}\right|^2, \quad 0 < f \leq \frac{1}{2\Delta t} \tag{7}$$

where $\Delta t = 1/f_s$, and f_s is the sampling frequency. The factor of 2 is included to conserve the total energy of the PSD. N is the length of the time series x_n. The periodogram calculation used a discrete Fourier transform (DFT) with 230,000 points.

Welch's method is a modified periodogram technique which reduces PSD variance (σ^2) by splitting the time series x_n into smaller segments and computing the modified (windowed) periodogram for each [18]. The windowed periodograms are then averaged to produce a PSD estimate with reduced variability. The modified periodogram is defined as follows:

$$PSD\left(\theta_j, f\right) = 2\frac{\Delta t}{N}\left|\sum_{n=0}^{N-1} h_n x_n e^{-j2\pi f \Delta t n}\right|^2, \quad 0 < f \leq \frac{1}{2\Delta t} \tag{8}$$

where h_n is a window function. Welch's method typically employs overlapping windows to prevent information loss at the edges of windows. A Hanning window with 50% window overlap was used for analysis. Each time series was divided into 32 segments, each segment comprising approximately 7187 samples. This segment size was used for all dimensional power spectra calculations. The SPL power spectra may then be calculated as:

$$SPL\left(\theta_j, f\right) = 10\log_{10}\left(\frac{PSD\left(\theta_j, f\right)}{{p_{ref}}^2}\right) \tag{9}$$

The PSD estimate was also examined using premultiplied spectra [19], with the goal of filtering noise to clearly show contributions of the blade pass frequency (BPF) harmonics. The PSD for premultiplied spectra was calculated with segments of length $N = 2f_s/\Omega$ where Ω is the rotational speed. This reduced variance for plot legibility, while still preserving the spectral content in the observed frequency ranges.The pre-multiplied spectra is given as:

$$G\left(\theta_j, f\right) = PSD\left(\theta_j, f\right) \cdot f/\sigma^2\left(x_n\right) \tag{10}$$

where $\sigma(x_n)^2$ is the variance of the original signal x_n [19]. The integral of PSD is given as:

$$\sigma^2\left(\theta_j\right) = \sum_{n=0}^{N-1} PSD\left(\theta_j, f\right)\delta f \tag{11}$$

where δf is the frequency resolution of the PSD, given as $\delta f = \frac{f_s}{N}$ where N is the segment length.

The overall sound pressure level (OASPL) may then be given as:

$$OASPL\left(\theta_j\right) = 10\log_{10}\left(\frac{\sigma^2\left(\theta_j\right)}{{p_{ref}}^2}\right) \tag{12}$$

The PSD of a specific frequency band may be calculated by changing the summation limits:

$${\sigma_{a-b}}^2\left(\theta_j\right) = \sum_{n=n_a}^{n_b} PSD\left(\theta_j, f\right)\delta f \tag{13}$$

Therefore, in the case of integrating from harmonic a to harmonic b, $n_a = \frac{a \cdot BPF}{\delta f}$ and $n_b = \frac{b \cdot BPF}{\delta f}$. The OASPL for a frequency band of BPF harmonics is then given by:

$$OASPL_{a-b}\left(\theta_j\right) = 10\log_{10}\left(\frac{{\sigma_{a-b}}^2\left(\theta_j\right)}{{p_{ref}}^2}\right) \tag{14}$$

Similarly, the OASPL for a single harmonic may be calculated by integrating over a small frequency range in the locus of the harmonic frequency:

$${\sigma_i}^2\left(\theta_j\right) = \sum_{n=n_i-2}^{n_i+2} PSD\left(\theta_j, f\right)\delta f \tag{15}$$

Here, $n_i = \frac{i \cdot BPF}{\delta f}$, which is the index of the ith BPF harmonic. The corresponding OASPL is then:

$$OASPL_i\left(\theta_j\right) = 10\log_{10}\left(\frac{{\sigma_i}^2\left(\theta_j\right)}{{p_{ref}}^2}\right) \tag{16}$$

The sound pressure data analyzed in this study showed clear correlations with the average recorded motor RPM, but the lack of a time-aligned record of the 1/rev data for the motor introduces some uncertainty with respect to the higher order harmonics. Additional noise and uncertainty at higher frequencies may also be associated with the product of motor angular speed and pole number. Ideally, the sound pressure time series would be indexed by the 1/rev data, thus allowing spectral analysis to be directly aligned with the periodicity of the rotor. The current aeroacoustic test bench does not have the capability for synchronized 1/rev data recording, however, so other approaches were taken to better understand the frequency content of the propeller SPL. Among these other approaches, the wavelet power spectra (WPS) scalogram was selected to provide qualitative analysis of the sound pressure signal [20].

The continuous wavelet transform (CWT) is a signal analysis method that is used to perform a time and scale decomposition of a signal. This method is analogous to the Fourier transform, but the analyzing function for the CWT is a wavelet, $\psi(t)$, as opposed to a complex exponential, $e^{j\omega t}$ [21]. The CWT involves the translation and dilation of this original "mother" wavelet to resolve the time-varying and/or the frequency-varying localized components of the analyzed signal [22]. A numerical version of the CWT as implemented in MATLAB® [23] through the `cwt()` function:

$$C(a,b) = \int_{-\infty}^{\infty} f\left(t\right)\frac{1}{a}\psi^*\left(\frac{t-b}{a}\right)dt \tag{17}$$

$C(a,b)$ are the wavelet transform coefficients, which are a function of the scale parameter a, and the position parameter b. The * operator signifies the complex conjugate. By varying a and b, the wavelet transform allows the original signal $f(t)$ to be analyzed at various scales.

For this analysis, the input signal $f(t)$ was the recorded pressure $p(t)$, and the selected wavelet function $\psi(t)$ was the Morse wavelet. The generalized Morse wavelet [24] is defined in the frequency domain as:

$$\Psi_{\beta,\gamma}\left(\omega\right) = U\left(\omega\right)a_{\beta,\gamma}\omega^{\beta}e^{-\omega^{\gamma}} \tag{18}$$

where $U(\omega)$ is the Heaviside step function and:

$$a_{\beta,\gamma} \equiv 2\left(\frac{e\gamma}{\beta}\right)^{\beta/\gamma} \tag{19}$$

Table 1 Propellers Tested

Propeller	Diameter (in.)	Pitch (in.)	Solidity
DJI Phantom Carbon	9.45	5	0.106
DJI Phantom Plastic	9.45	5	0.106
Master Airscrew MR 9×4.5	9.45	5	0.118

There are numerous other wavelets available for analysis, each with relative merits [19, 20, 22, 24], but the Morse wavelet is well-supported by the `cwt()` function [25] and can be configured for different use cases. The generalized Morse wavelet is parameterized with the time-bandwidth product, $P^2 = \beta\gamma$:

$$\Psi_{P,\gamma}(\omega) = U(\omega)\, a_{P,\gamma}\omega^{\frac{P^2}{\gamma}} e^{-\omega^{\gamma}} \tag{20}$$

γ is the measure of skewness of the wavelet, with a value of 3 corresponding to a symmetric waveform. By holding γ constant at 3, and increasing the time-bandwidth product, the wavelet frequency resolution may be increased at the expense of time resolution [25]. As this study is primarily focused on the frequency content of UAV propeller noise under static conditions, the average frequency content (as presented in a periodogram) is desired. However, due to inconsistencies relating to the test setup and lack of 1/rev motor data, a Morse wavelet with $\gamma = 3$ and $P^2 = 60$, was used to provide a balance of frequency resolution and time resolution throughout the analyzed signal.

The `cwt()` function calculates the wavelet coefficients $C(a, b)$ using L1 normalization [23] using the discretized form of Eq 17. The WPS is then computed as:

$$E(l,t) = \frac{|C(l,t)|^2}{l} \tag{21}$$

However, as the `cwt()` function returns L1 normalized results, the scale term l is dropped. Thus, the WPS in frequency terms is calculated as:

$$E(f,t) = |C(f,t)|^2 \tag{22}$$

where $C(f,t)$ are the L1 normalized coefficients returned by MATLAB. The associated SPL can then be calculated as:

$$SPL(f,t) = 10\log_{10}\left(\frac{E(f,t)}{{p_{ref}}^2}\right) \tag{23}$$

This method for calculating WPS and associated SPL is similar to that presented in Tinney and Sirohi [19]. The SPL values may then be visualized in a scalogram plot to qualitatively examine the spectral content of the signal resolved in both time and frequency.

For all frequency related plots, frequency, f has been presented in terms of blade pass frequency:

$$f^{+} = \frac{f}{BPF} \tag{24}$$

This non-dimensional frequency allows for the comparison of data sets collected at different RPMs.

C. Propellers Tested

Three propellers were tested for this paper: DJI Phantom Carbon, DJI Phantom Plastic, and Master Airscrew MR 9.4×4.5. The DJI propellers are manufactured by DJI and are designed for the Phantom quadrotor. The Master Airscrew propeller is marketed as a replacement propeller for the Phantom. Table 1 provides a summary of the three propellers. The diameter provided is the true diameter and was the value used in calculations. The pitch is the value provided by the manufacturer. The solidity was calculated from the chord distribution of the propellers.

The chord and twist distribution for each propeller was measured using the PropellerScanner software created by Hepperle [26]. With this software, pictures of the front and side of the propeller are used to determine the chord and twist distributions. Uhlig, et al. [27, 28] showed that the PropellerScanner software provided an accurate measure of the chord distribution but can underestimate the twist angles. While the twist measurement from PropellerScanner might

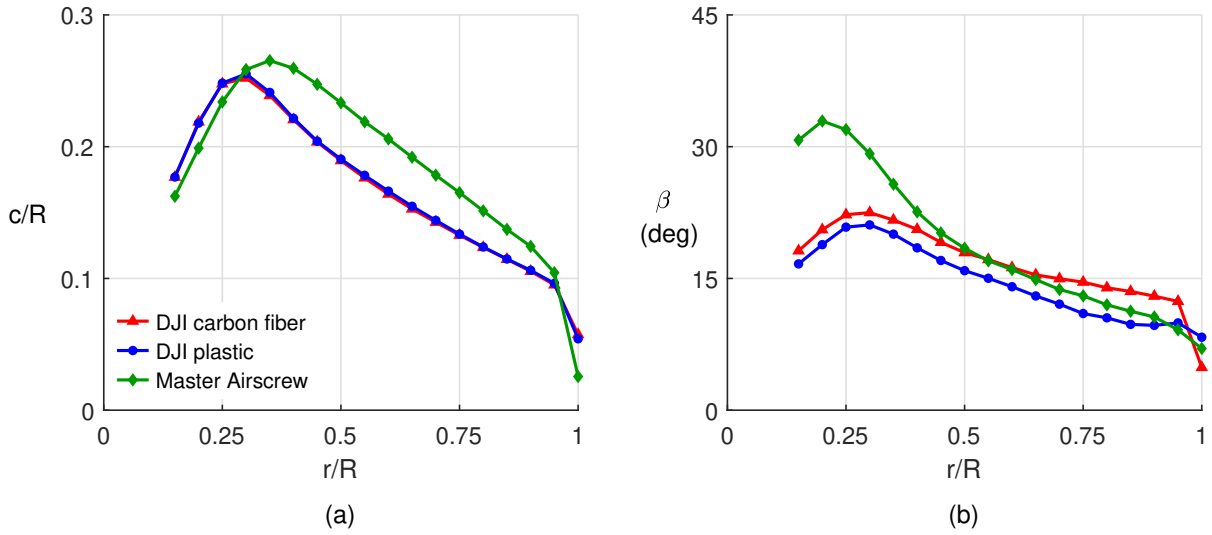

Fig. 6 Propeller geometry: (a) chord distribution (b) twist distribution.

not be as accurate as physically measuring the angle, the software does provide an easy way to compare the geometries of different propellers. Figure 6(a) provides the chord distribution of the propellers and Fig. 6(b) provides the twist distribution. The two DJI propellers have the same chord distribution, but the carbon propeller has a greater pitch than the plastic. The Master Airscrew propeller has a larger chord than the DJI propellers over most of the blade radius. The twist for the Master Airscrew is larger for the first half of the blade radius but then falls between the DJI carbon and DJI plastic in the outer portion of the blade.

III. Results

This section presents the aerodynamic performance data, aeroacoustic behaviors, and correlation between the aerodynamic and acoustic behavior for the three propellers.

A. Aerodynamic Performance

The static performance of the three propellers used in this study is shown Fig. 7. As seen in the figure, the Master Airscrew propeller had the largest static thrust coefficients but also produced the largest power coefficients. The DJI carbon propeller had the next largest thrust and power coefficients, and the DJI plastic propeller had the smallest thrust and power coefficients. Each propeller saw an increase in their thrust coefficient as the RPM increased. This behavior is a common Reynolds number effect in small-scale propellers [2]. The DJI plastic and Master Airscrew propellers saw a small decrease in their power coefficient as the RPM increased while the DJI carbon was mostly constant.

The geometry of the propellers (Fig. 6) explains the relative magnitudes of the thrust and power coefficients (Master Airscrew with the largest, then DJI carbon, and finally DJI plastic with the smallest). While the DJI propellers have the same chord distribution, the twist angles of the carbon propeller are larger. These larger angles are the reason for the larger thrust and power coefficients for the carbon propeller over the plastic propeller. For the Master Airscrew propeller, its larger chord distribution is the reason for its larger thrust and power coefficients.

Since each propeller has a different thrust coefficient, the RPM required for each propeller to produce a specific thrust will be different. Figure 8 shows the thrust produced from each propeller as a function of RPM. To demonstrate the differences in RPM from each propeller, the minimum thrust required from a propeller to maintain steady hovering flight of a DJI Phantom 3 will be used as an example. The Phantom 3 has a weight of about 2.8 lb, so a single propeller for this quadrotor would need to produce 0.7 lb of thrust for steady hovering flight (assuming no thrust losses from the airframe or propeller interference). A thrust of 0.7 lb is shown in Fig. 8, and it is seen that the Master Airscrew would need an RPM around 4500, the DJI carbon would need around 4800, and the DJI plastic would need around 5200.

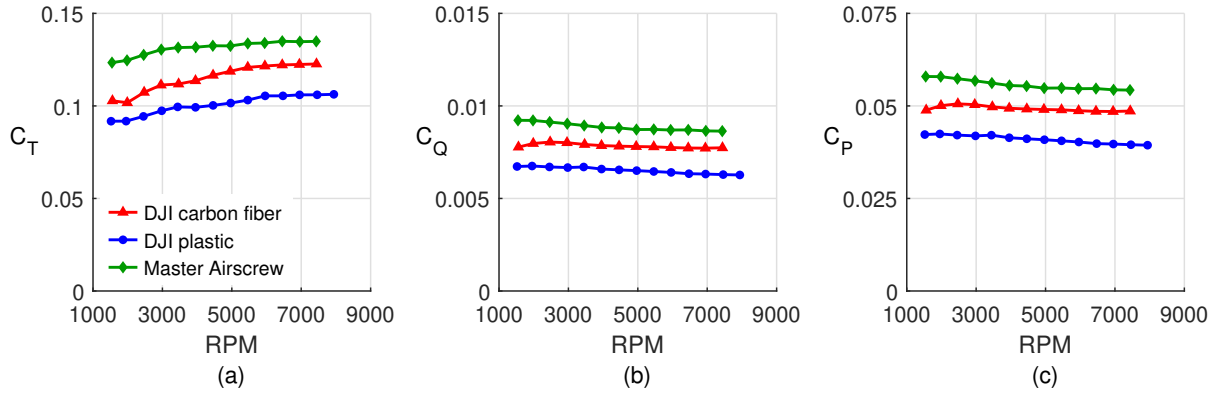

Fig. 7 Aerodynamic performance: (a) C_T vs RPM, (b) C_Q vs RPM, and (c) C_P vs RPM.

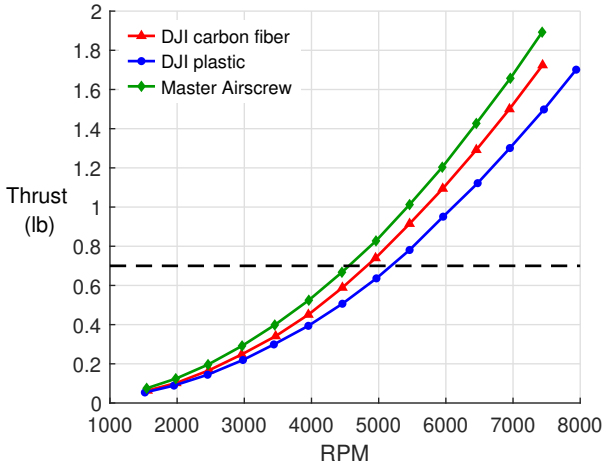

Fig. 8 Thrust performance.

B. Aeroacoustic Characteristics

1. Aeroacoustic Data Validation

While the static aerodynamic data has been previously validated [2–4], the aeroacoustic test bench was recently designed and tested, thereby necessitating a data validation procedure. Figure 9 compares the SPL spectral data of the DJI carbon fiber propeller at an RPM of 5300 with results from Yang et al. [29]. Yang et al. utilized a similar test setup as was used in this study with a DJI Phantom 2 propeller and motor. Figure 9(a) co-plots the reference data with the experimental results subjected to the Welch data reduction algorithm while Fig. 9(b) shows the experimental data subjected to the periodogram analysis. While both methods capture the SPL peaks to a good degree of accuracy, the periodogram method results in significant noise, specifically at the higher frequencies, while the Welch's method predicts clear, distinguishable peaks. Based on the above results, the Welch's algorithm is used for calculating the power spectral density estimates for all subsequent analyses.

2. Baseline Case Analysis

In order to get a better understanding of the acoustic contributions of the various systems involved, including but not restricted to the propeller, motor, speed controller, and the test-bench vibrations, separately and in conjunction, the DJI carbon fiber propeller operating at an RPM of 5300 is chosen as the baseline case and is subjected to a power spectral density, premultiplied spectra, and wavelet power spectra analysis.

Figure 10 shows the SPL spectra for the motor operating with and without the propeller, plotted against the non-dimensional blade pass frequency, f^+, at the (a) in-plane (0 degree observer) and (b) out-of-plane (−90 degree observer) positions. When studying the acoustic spectra of the motor alone, a clear peak in SPL can be identified around

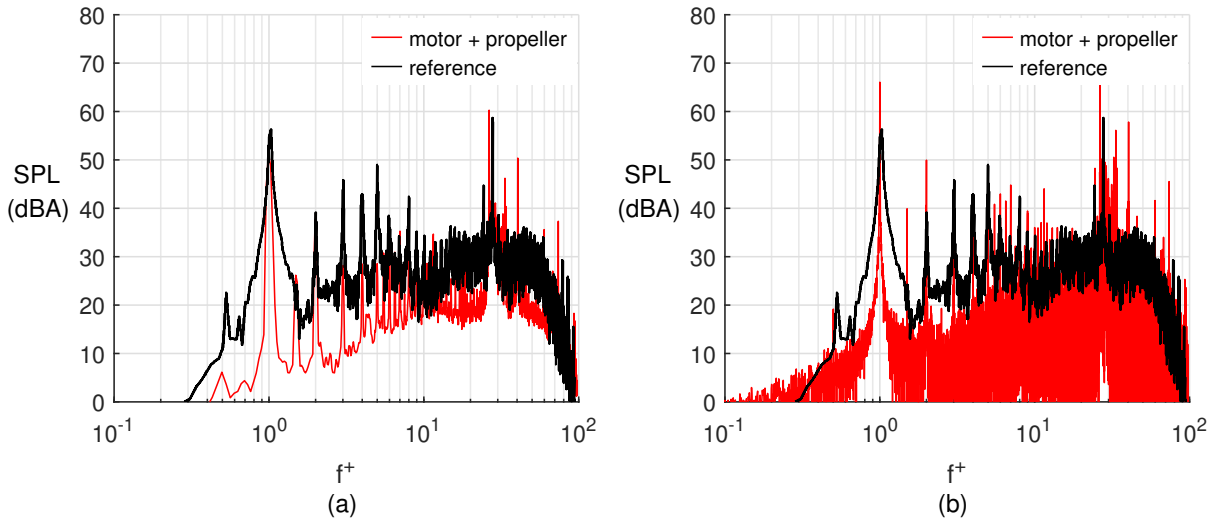

Fig. 9 Aeroacoustic data calculated using (a) Welch's method, and (b) standard periodogram.

$f^+ = 0.5$, corresponding to the motor shaft frequency, f_{shaft} (half of BPF for 2 bladed propellers). This is followed by several peaks around the 6th and 7th BPF harmonics and considerable variance in the higher harmonics. An examination of the peak harmonics on a linear frequency scale in Figure 11 allows peak locations at higher harmonics to be identified. The sequence of peaks observed around the 6th harmonic occur approximately at $f^+ = 6$, 6.5, 7, and 7.5 respectively. The 7th BPF harmonic corresponds to the 2nd harmonic of motor supply current line frequency $f_l = N \cdot f_{shaft}$ [30], where N is the number of pole pairs in the BLDC motor, and N = 7 for the DJI 2312 motor. Motor SPL recorded for this study exhibits significantly more variability than the results obtained by Henderson and Huff for the DJI 2312 motor, but the locations of significant peaks appear to match the results of that study. The four peaks around the 7th BPF harmonic correspond to dimensional frequency values of approximately 1000, 1100, 1200, and 1300 Hz, which are attributed to shaft eccentricity noise by Henderson and Huff. Another notable peak described by Henderson and Huff occurs around 5000 Hz at 5370 RPM, attributed to motor resonance. This corresponds to the region at and surrounding $f^+ = 27.5$ in Figure 11 (a), suggesting that motor resonance may be a source of noise at higher BPF harmonics. Additional variance in the motor SPL spectra may also be due to noise resulting from the vibrations and instabilities of the acoustic test bench.

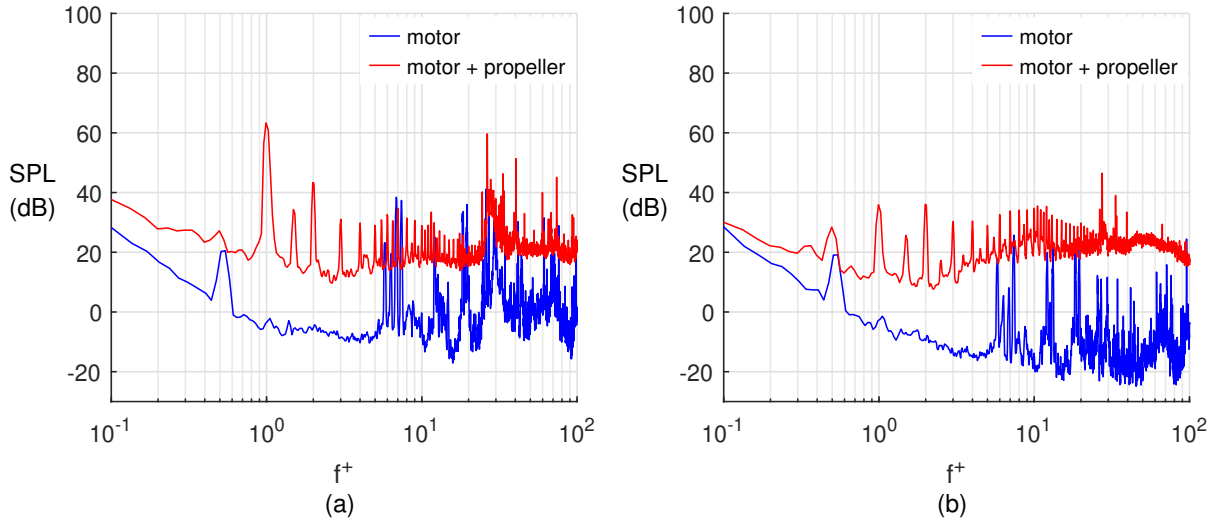

Fig. 10 DJI carbon fiber propeller at 5300 RPM: SPL spectra of motor and (motor + propeller) data for the (a) in-plane (θ = 0°), and the (b) out-of-plane (θ = -90°) stations.

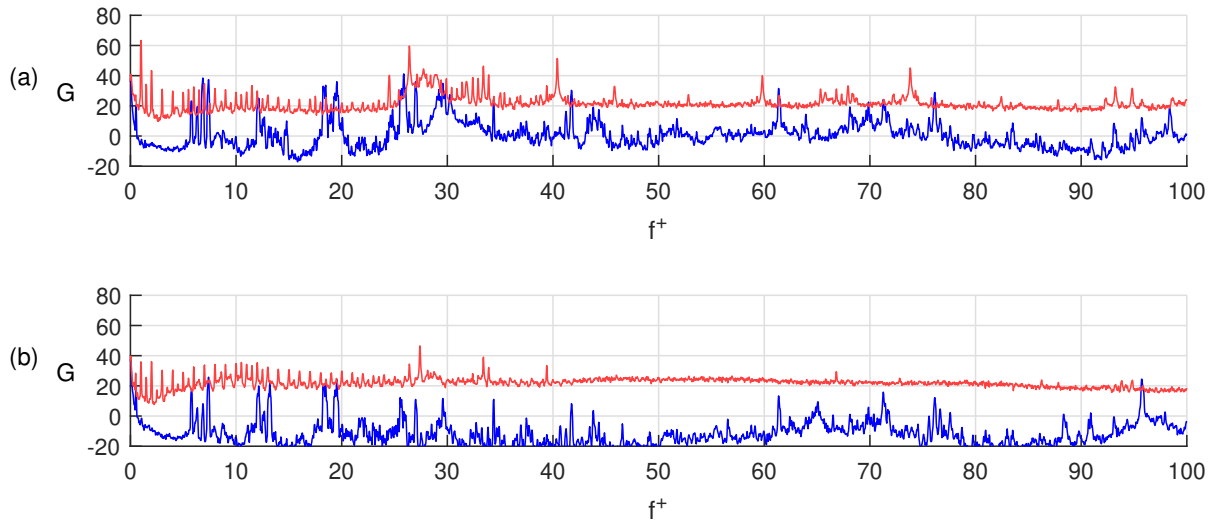

Fig. 11 DJI carbon fiber propeller at 5300 RPM: SPL spectra (linear frequency scale) of motor and (motor + propeller) data for the (a) in-plane (θ = 0°), and the (b) out-of-plane (θ = -90°) stations.

Addition of the propeller to the system results in clear peaks at the fundamental blade pass frequency with subsequent, decaying peaks at the 2nd and 3rd harmonic, as observed in Fig. 10(a). Subsequent peaks at BPF harmonics and subharmonics corresponding to f_{shaft} are identifiable up to approximately f^+ = 25 for both observation locations. For $f^+ > 25$, peaks exhibit the same periodicity ($\Delta f^+ \approx 0.5$), but peaks no longer align exactly with BPF harmonics or shaft frequency harmonics, and diverge further with increasing values of f^+. This suggests that the recorded RPM slightly exceeds the actual RPM, resulting in values of f^+ that slightly lag BPF harmonics and subharmonics.

Following the 2nd and 3rd harmonic peak, harmonic peaks exhibit similar prominence to the third harmonic until the 7th peak, which exhibits a slightly higher SPL. This is in agreement with the observed peaks in motor SPL around the 7th BPF harmonic, suggesting that this peak is attributed to motor noise. The second largest peak occurs at approximately f^+ = 26.5 in Figure 11 (a), and f^+ = 27.5 in Figure 11 (b), which does not correspond to BPF harmonics or line frequency harmonics. However, this frequency does correspond to the resonance frequency observed in the motor SPL spectra. [30] Other significant peaks in SPL are located at f^+ = 33.5, 40.5, 60, and 74, which may be due to other resonant modes in the test setup. The higher order harmonics are therefore considered as "nonrotor" harmonics henceforth, as the aeroacoustic contributions at these higher frequencies have not been verified at this time. Introduction of the propeller also adds a broadband noise to the system due to turbulent inflow and the boundary-layer interactions of the propeller with its own wake.

Premultiplied spectra plots for the combined motor and propeller system as detected from the in-plane and out-of-plane locations, shown in Fig. 12, provide a clearer picture of the prominent noise sources in the baseline case study. For the in-plane observer (Fig. 12(a)), SPL peaks at f^+ = 1, 26.5, 40.5, and 74 are the main identifiable sources of noise. The peak at the fundamental BPF harmonic can be attributed to the propeller, but the higher harmonics are likely due to motor noise or structural vibrations when cross-referenced with the SPL spectra in Fig. 10(a). For the out-of-plane observer, the only prominent peaks are located at f^+ = 27.5 and 33.5, and are likely due to motor resonance noise.There is almost zero energy at and close to the fundamental frequency. Overall, while the in-plane and out-of-plane premultiplied spectral data can be used to clearly distinguish between the noise emanating from the propeller and test-bench vibrations, it is clear that the motor and structural noise at the higher harmonics are the dominant noise source from a detection stand point, regardless of observation location.

A time frequency analysis was carried out on the baseline case to determine the stability of the system and ascertain potential areas of improvement of the aeroacoustic test bench. WPS scalograms were generated and plotted (in Fig. 13) for 4.8 s of audio data from the two microphones, extracted from the middle of the data set where the system could safely be assumed to be operating nominally. Figure 13(a) shows that the SPL amplitude at the 1st and 2nd harmonics, as well as in the frequency band between the 25th through 30th harmonics, remains consistent with time. Time dependent fluctuations are observed close to and beyond the 30th harmonic. Similar observations in the time-dependent power spectra can be made from the out-of-plane station (Fig. 13(b)), further pointing to the instabilities likely resulting from

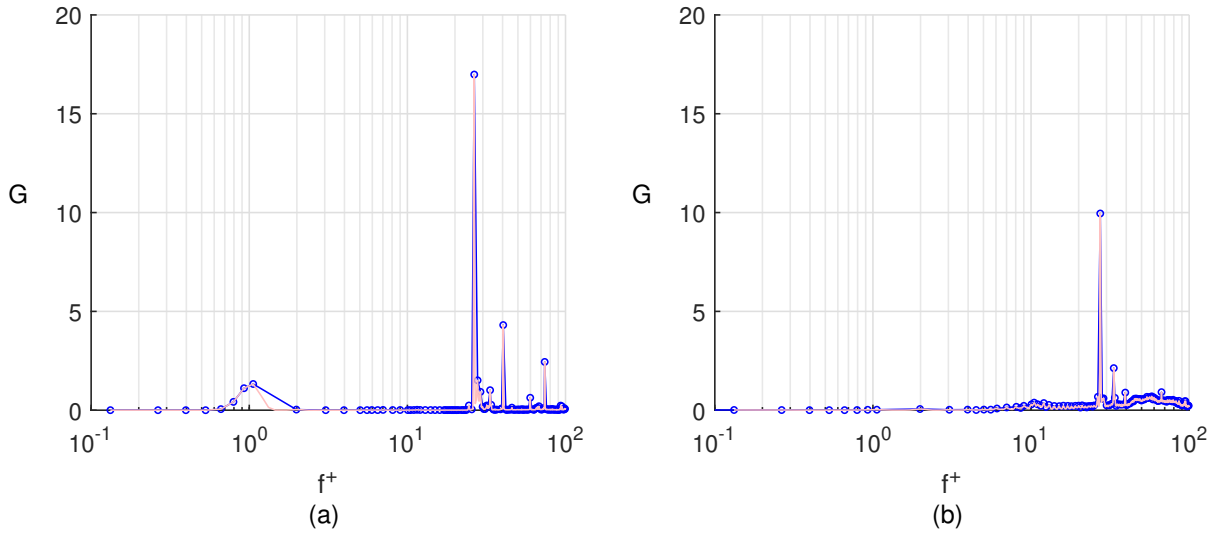

Fig. 12 DJI carbon fiber propeller at 5300 RPM: Premultiplied spectra for the (a) in-plane (θ = 0°), and the (b) out-of-plane (θ = -90°) stations.

test-bench vibrations and speed controller noise. Additionally, Fig. 13 shows that an observer at the in-plane location is subjected to more noise across a broad spectrum of frequency when compared to an observer at the out-of-plane location.

While the authors recognize that the nonrotor noise sources, specifically due to test-bench vibrations, are not ideal, the high frequency of said contributions (greater than 25 times the blade pass frequency) should not affect the conclusions drawn in subsequent sections based on the harmonic noise of the propeller at the lower blade pass frequencies that relate to the blade geometry and surface aerodynamic loading. Further iterations of the current research will focus on eliminating the nonrotor noise by using a quieter motor, muffling the sound of the speed controller, and significantly dampening the vibrations of the test bench in order to better understand the affect of the harmonic and broadband noise contributions of the propeller.

3. Power Spectra Analysis for Variation in RPMs and Propeller Geometry

In the current section, the variation in the acoustic characteristics of the DJI carbon fiber propeller with change in RPM is analyzed. Additionally, the general acoustic behavior of the DJI plastic and Master Airscrew propellers are compared with that of the DJI carbon fiber propeller.

Figures 14–16 plot the SPL versus f^+ data at the (a) in-plane and (b) out-of-plane locations at five RPMs for the DJI carbon fiber, DJI plastic, and Master Airscrew propellers, respectively. Figure 14(a) demonstrates that the harmonic noise at the fundamental blade pass frequency increases with increasing RPM, from a minimum value of 51 dB at 3000 RPM to a maximum value of 73 dB at 7900 RPM. A similar, increasing trend in peak SPL is observed as the frequency increases from the 2nd to the 5th blade harmonic, consistent with trends observed in literature [19, 31]. The SPL behavior starts to deviate somewhat in the vicinity of the 7th, 12th, and 18th harmonics, where noise contributions of the motor are more pronounced. Above the 25th harmonic, rotor noise can still be identified at some BPF harmonics, but the majority of noise generated at this frequency appears to be due to motor and structural vibrations. As such, no apparent trend for these higher harmonics can be established with increasing rotation speeds.

This lack in trend is highlighted by analyzing the behavior of the SPL peak at the harmonic associated with the motor noise. For RPM$\leq$ 5300, the peak SPL due to motor noise occurs at around the 54th, 41st, and 26th harmonic for the 3000, 3900, and 5300 RPM cases, respectively. This decrease in peak SPL f^+ can be attributed to increasing dimensional frequency, as the dimensional frequency of these peaks remains close to 5000 Hz for RPM$\leq$ 5300. Above 5300 RPM, there is no clear single peak of nonrotor noise. Peak SPL magnitude at higher harmonics increases from 3000 to 3900 RPM but then decreases with increasing RPM. The lack of an apparent trend at the higher rotational speeds can possibly be attributed to the instabilities in the test-bench structure (as discussed in Section III.B.2), which tend to fluctuate with propeller rotation speed, leading to chaotic SPL behavior at said harmonics. While similar trends

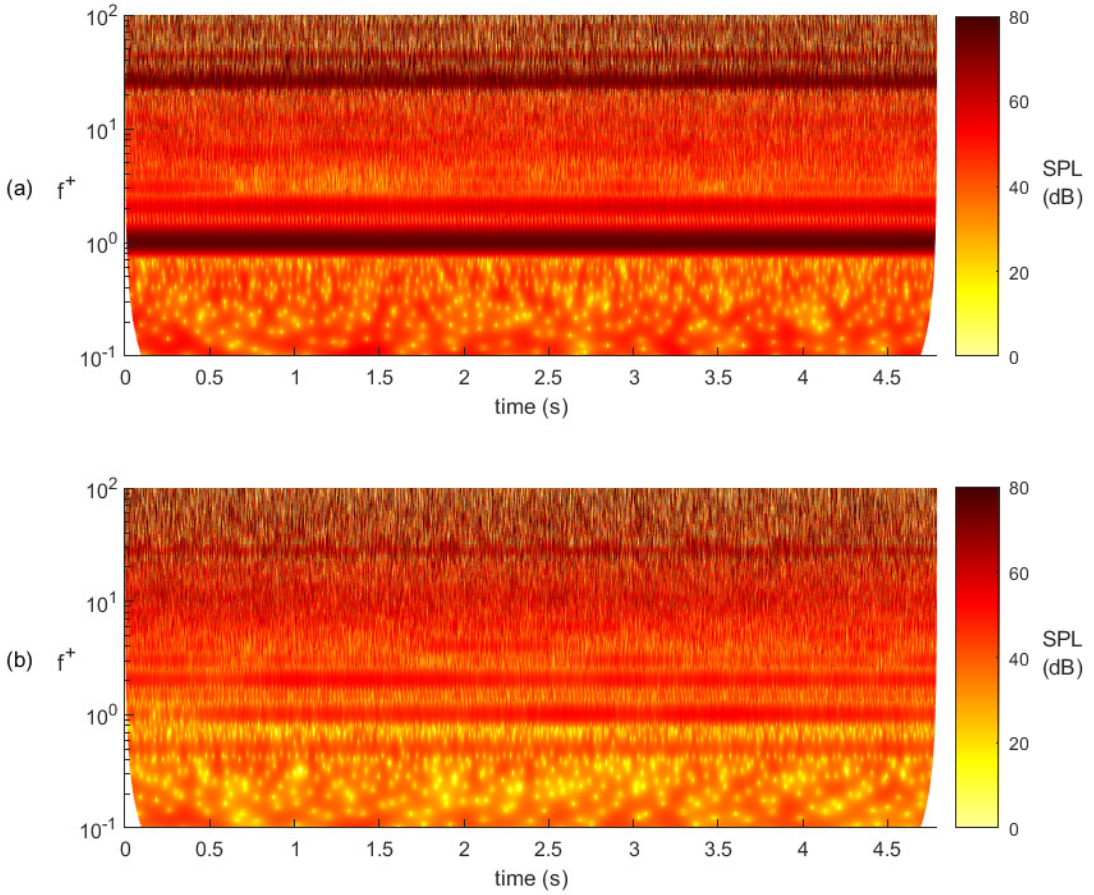

Fig. 13 DJI carbon fiber propeller at 5300 RPM: WPS scalogram for the (a) in-plane (θ = 0°), and the (b) out-of-plane (θ = -90°) stations.

in harmonic noise are observed at the out-of-plane station (Fig. 14(b)), overall broadband noise contributions at both observation locations are seen to increase with increasing rotational speeds.

SPL spectra of the DJI plastic and Master Aisrscrew propellers (Figs. 15 and 16) show similar behavior in propeller harmonic and broadband noise contributions when compared to those observed for the DJI carbon fiber propeller (Fig. 14) with two main exceptions: (i) the minor SPL peaks at the sub-harmonic, below the fundamental blade pass frequency, are greater in magnitude and (ii) the propeller noise contributions are higher, and the motor noise contributions are lower, for the Master Airscrew propeller as compared to the DJI carbon fiber and plastic propellers, evidenced by the peak SPL values at the fundamental and motor noise harmonics, respectively.

Due to the issues with test bench vibrations affecting the acoustic data at the higher blade harmonics, efforts are made to analyze the variation in noise levels with rotational speeds at the lower harmonics associated with the propeller noise (up to the third blade pass frequency), higher harmonics associated with the nonrotor noise and less significant rotor noise (above the third blade pass frequency), and the full harmonic range (all blade pass frequencies), separately. Figure 17 plots the effect of propeller rotational speed on the noise level contributions due to the (a) propeller harmonic noise, (b) nonrotor, and (c) combined harmonics for the DJI carbon fiber, DJI plastic, and Master Airscrew propellers at the in-plane (top row) and out-of-plane (bottom row) observation stations. For an in-plane observer, independent of propeller geometry, the noise contribution due to the propeller increases with increase in rotational speeds, as observed in Fig. 17(a). OASPL levels at the propeller harmonics are the same for all propellers, with a marginally small noise reduction for the DJI plastic propeller at higher RPMs. Given that the geometry of these propellers are similar, this behavior is expected. Similar trends in propeller OASPL are observed at the out-of-plane station (Fig. 17(d)) with the

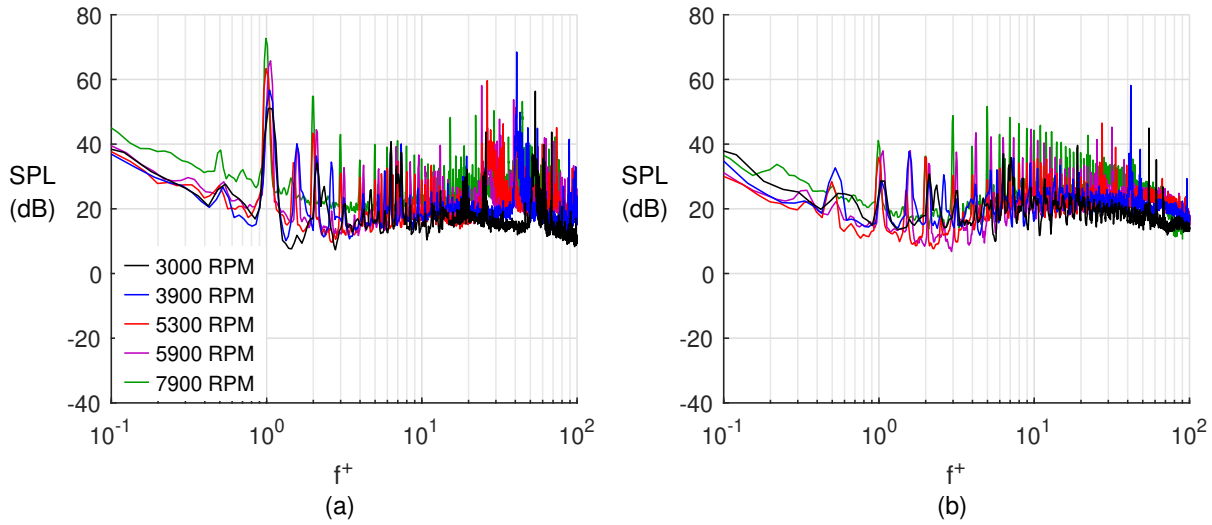

Fig. 14 DJI carbon fiber propeller: SPL spectra for the (a) in-plane (θ = 0°), and the (b) out-of-plane (θ = -90°) stations.

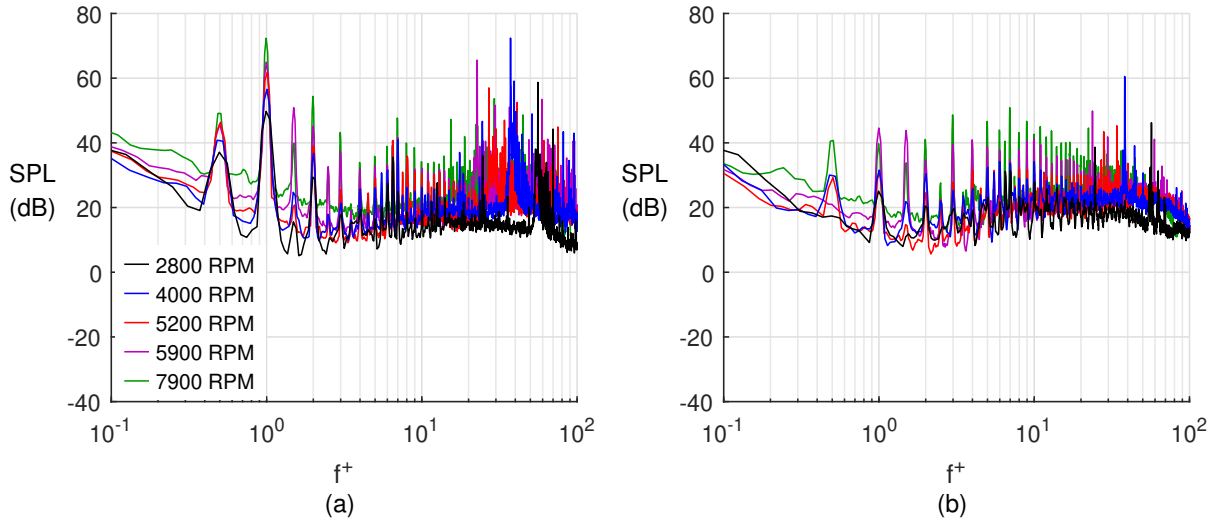

Fig. 15 DJI plastic propeller: SPL spectra for the (a) in-plane (θ = 0°), and the (b) out-of-plane (θ = -90°) stations.

exception of a sudden increase in noise levels at the lower RPM conditions. This non-linearity at the lower rotational speeds could be an outlier caused due to the acoustic instabilities and needs to be explored further in future work.

On comparing the variation in nonrotor noise levels with RPM in Fig. 17(b) and (e) at both observation stations, no generic trend can be established for any of the propellers. This non-linear behavior can be attributed to the spurious noise introduced as a result of the test-bench vibrations. Therefore, detailed conclusions on the nonrotor and overall noise contributions (Fig. 17(c) and (f)) for varying propeller geometry and aerodynamic performance conditions in the current and following sections are not made.

C. Correlation between Propeller Aerodynamics and Aeroacoustics

The relationship between the propeller performance parameters and the acoustics is explored in the current section. Section III.C.1 analyzes the variation in OASPL levels due to propeller in terms of the thrust produced. The OASPL directivity patterns for the first two blade harmonics are studied in Section III.C.2 and correlated with the propeller geometry and loading.

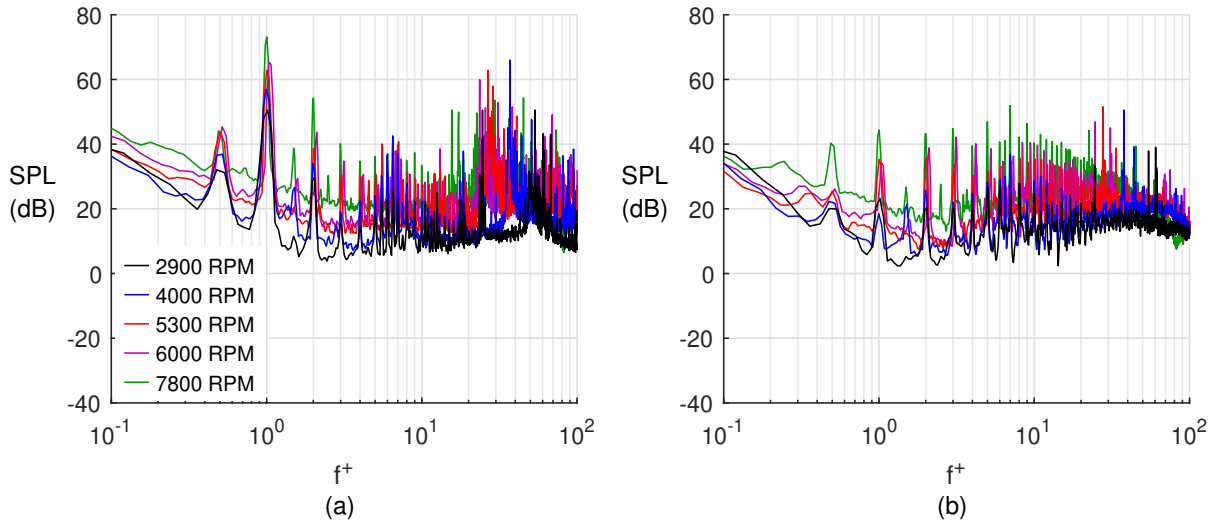

Fig. 16 Master Airscrew propeller: SPL spectra for the (a) in-plane (θ = 0°), and (b) out-of-plane (θ = -90°) stations.

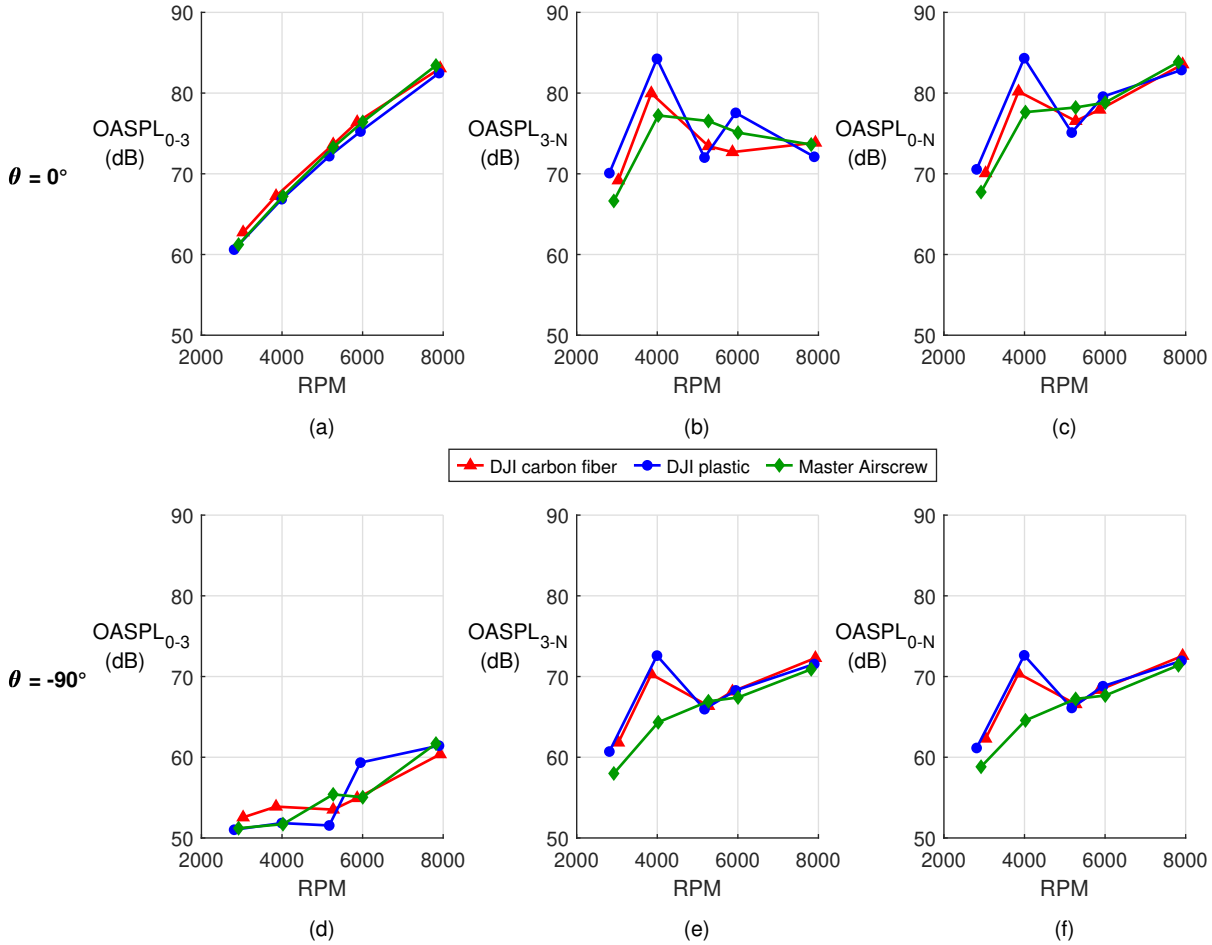

Fig. 17 OASPL variation with RPM (a) in-plane (θ = 0°), and (b) out-of-plane (θ = -90°) stations.

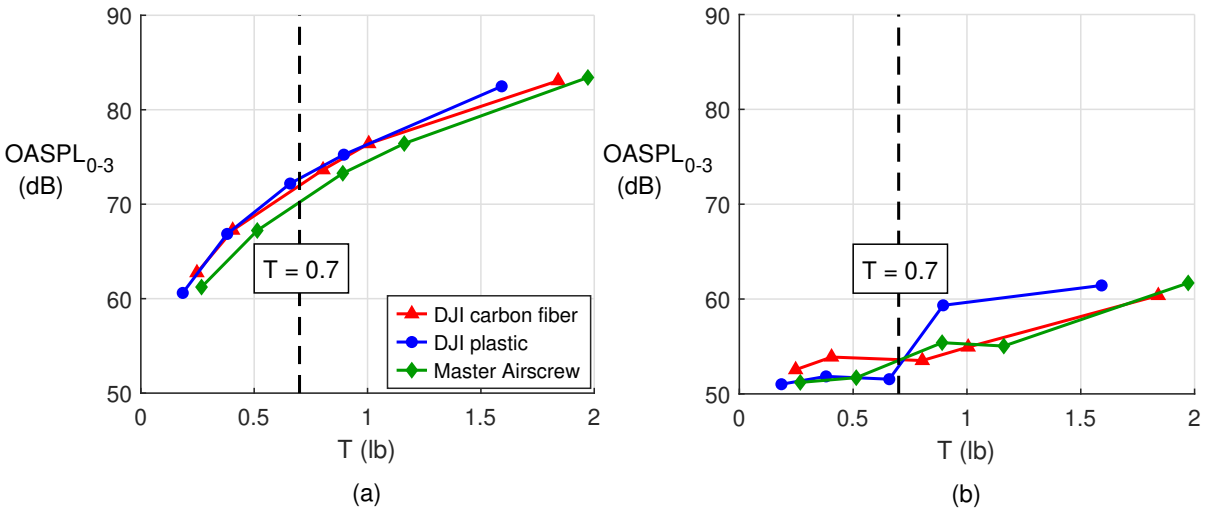

Fig. 18 Low frequency OASPL ($0 \leq f^{+} \leq 3$) vs thrust: (a) in-plane and (b) out-of-plane.

1. OASPL Variation with Aerodynamic Performance Metrics

As discussed earlier, the in-plane OASPL for the propellers (first three harmonics) increased with RPM, and each propeller had about the same OASPL at each RPM. From the aerodynamic performance discussion of the propellers (Section III.A), the Master Airscrew propeller had the largest C_T of the three. This larger C_T means that the Master Airscrew will spin at a lower RPM to produce the same thrust as the other two propellers (Fig. 8). With this information in mind, the OASPL for the propellers (first three harmonics) was plotted against the thrust produced by the propellers (Fig. 18). The in-plane results (Fig. 18(a)) show that at a given thrust value, the Master Aircrew produces less noise (the dotted line is at 0.7 lb, which is the same example previously used). The reason that the Master Airscrew produces lower noise at a given thrust is because it is spinning at a lower RPM. Even though the DJI carbon had a larger C_T than the DJI plastic and therefore would spin at a lower RPM for a given thrust, the results from Fig. 18(a) show that for thrust values below 1 lb, the noise from the DJI carbon and DJI plastic are about the same at a given thrust.

Results from the out-of-plane OASPL (Fig. 18(b)) do not show a clear trend. At the 0.7 lb thrust, the three propellers all have about the same OASPL, but at larger thrust values, there is a large increase for the DJI plastic. More testing is needed to further investigate the out-of-plane noise behavior.

2. OASPL Directivity

Directivity patterns at the fundamental and 2nd harmonics can be valuable in determining the effect of blade thickness and loading on the propeller aeroacoustics. Figure 19 plots the OASPL levels at the first two blade pass frequencies, with each row representing the data for a single propeller. On comparing the directivity patterns at the first harmonic, we observe that the slopes at all rotational speeds are higher for the Master Airscrew propeller and lower and similar for the DJI propellers, pointing to the fact that the thickness noise is higher for the Master Airscrew propeller as compared to the other propellers. These observations are valid as the solidity of the Master Airscrew propeller (= 0.118) is higher that that of the DJI propellers (= 0.106).

Directivity patterns at the second harmonic show a sharp drop in noise levels as the observer moves from the in-plane to the out-of-plane position. Additionally, the OASPL for a given rotational speed is generally the highest for the Master Airscrew propeller, followed by the DJI carbon fiber and plastic propellers, respectively. These observations suggest that the loading noise contributions of the Master Airscrew propeller are the highest among the propellers considered in the current study.

IV. Conclusions

Characterization of the aerodynamics and aeroacoustics of small UAV propellers are necessitated by the increased demand for high performance drones. The current work aims to test the acoustics of small propellers and relate the data to the propeller's aerodynamics using static performance results from previous research. Initial efforts were focused

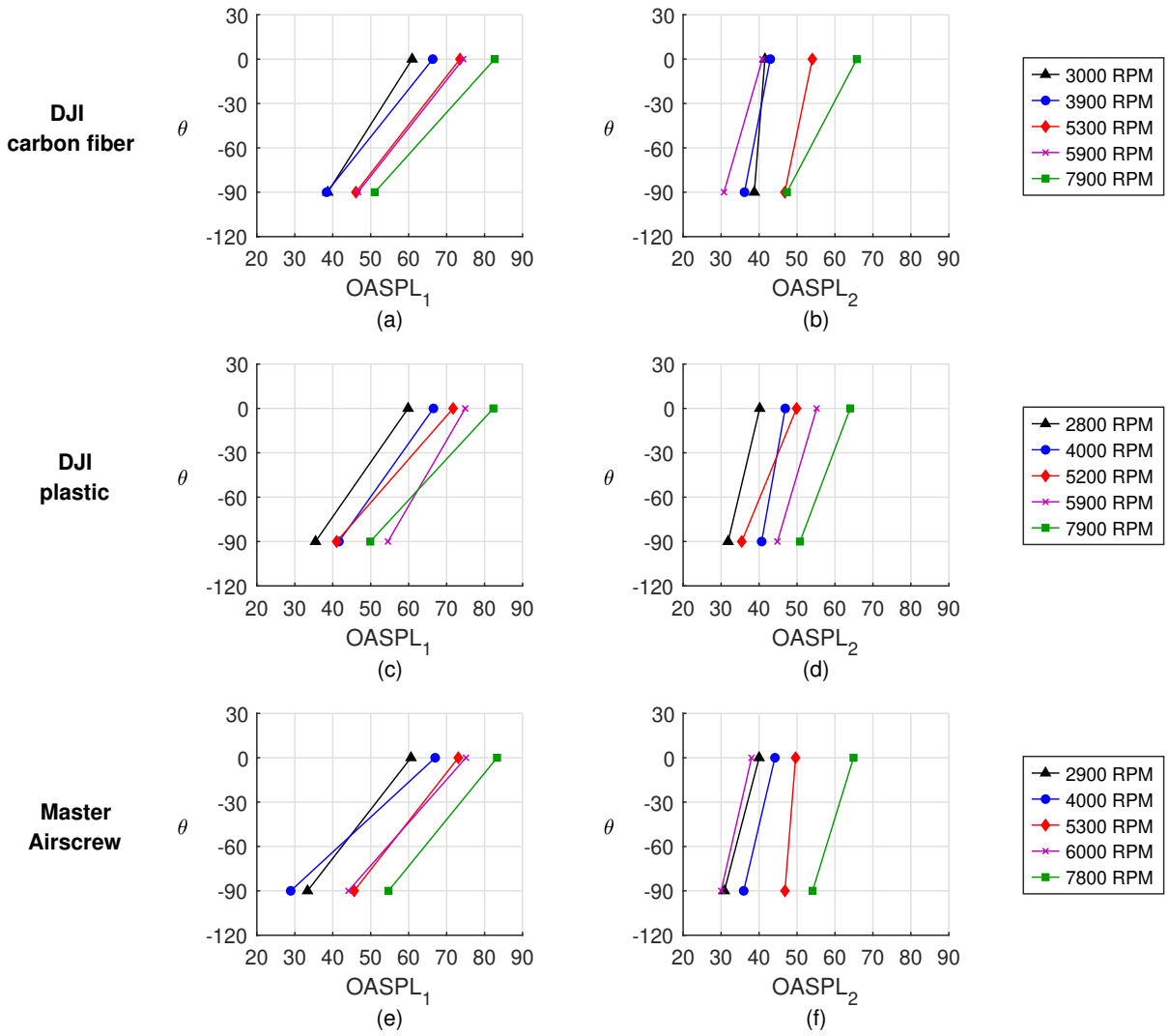

Fig. 19 OASPL Directivity for first two harmonics.

on designing, testing, and successfully validating an aeroacoustic test bench. Spectral, premultiplied spectra, and time frequency analysis for a baseline case indicated increased nonrotor noise at the higher frequencies, attributed to instabilities in the test bench. However, noise levels at the lower harmonics were captured with good accuracy and conclusions are only drawn at the associated harmonics.

Results indicated that low-harmonic OASPL increased with increase in RPM but only marginally varied between the propellers tested. When the amount of thrust produced by each propeller was considered, the Master Airscrew propeller produced the least amount of noise at a given thrust. The reason for the lower noise with the Master Airscrew was because it could spin at a lower RPM to produce the same thrust as the DJI propellers. OASPL directivity patterns at the first two blade pass frequencies showed that the thickness and loading noise contributions of the Master Airscrew propeller was the highest, followed by the DJI carbon fiber and plastic propellers, in that order.

Future research will focus on reducing the vibrations in the aeroacoustic test bench by utilizing dampeners, using a quieter BLDC motor to reduce motor noise, and muffling the sound due to the speed controller. Furthermore, detailed aeroacoustic experiments will be conducted for several small UAV propellers with varying material, pitch, diameter, and blade thickness in order to better understand and establish the relationship between the aerodynamics and aeroacoustics of small propellers and formulate holistic design approaches for efficient, small-scale UAV propellers.

References

[1] Christian, A. and Cabell, R., "Initial Investigation into the Psychoacoustic Properties of Small Unmanned Aerial System Noise," AIAA Paper 2017-4051, 2017.

[2] Deters, R. W., Ananda, G. K., and Selig, M. S., "Reynolds Number Effects on the Performance of Small-Scale Propellers," AIAA Paper 2014-2151, 2014.

[3] Deters, R. W., Kleinke, S., and Selig, M. S., "Static Testing of Propulsion Elements for Small Multirotor Unmanned Aerial Vehicles," AIAA Paper 2017-3743, 2017.

[4] Deters, R. W., Kleinke, S., and Selig, M. S., "Static Performance Results of Propellers Used on Nano, Micro, and Mini Quadrotors," AIAA Paper 2018-4122, 2018.

[5] Brandt, J. B. and Selig, M. S., "Propeller Performance Data at Low Reynolds Numbers," AIAA Paper 2011-1255, 2011.

[6] UIUC Propeller Database, https://m-selig.ae.illinois.edu/props/propDB.html, Accessed October 30, 2019.

[7] Merchant, M. P. and Miller, L. S., "Propeller Performance Measurement for Low Reynolds Number UAV Applications," AIAA Paper 2006-1127, 2006.

[8] McCrink, M. H. and Gregory, J. W., "Blade Element Momentum Modeling of Low-Reynolds Electric Propulsion Systems," *Journal of Aircraft*, Vol. 54, No. 1, 2017, pp. 163–176.

[9] Wisniewski, C.F., Byerley, A.R., Van Treuren, K.W., and Hays, A., "Experimentally Testing Commercial and Custom Designed Quadcopter Propeller Static Performance and Noise Generation," AIAA Paper 2017-3711, 2017.

[10] Huff, D.L. and Henderson, B.S., "Electric Motor Noise from Small Quadcopters: Part I Acoustic Measurements," AIAA Paper 2018-2952, 2018.

[11] Cambray, A., Pang, E., Ali, S.A.S., Rezgui, D., Azarpeyvand, M., "Investigation Towards a Better Understanding of Noise Generation from UAV Propellers," AIAA Paper 2018-3450, 2018.

[12] Yang, Y., Li, Y., Liu, Y., Arcondoulis. E.J.G., Wang, Y., Huang, B., and Li, W., "Aeroacoustic and aerodynamic investigation of multicopter rotors with serrated trailing edges," AIAA Paper 2019-2523, 2019.

[13] van Dommelen, D., Yang, M., Liu, W., Eppler, J., Darrah, D., and Anemaat, W.A.J., "UAV Rotor Acoustic Analysis and Optimization," AIAA Paper 2019-2547, 2019.

[14] Britcher, C.P., Landman, D., Duvall, B., Dodda, V.K.R., Lowe, C., Patel, Mihir., "An Aeroacoustic Study of Propellers for Small Electric Propulsion Aircraft," AIAA Paper 2017-3710, 2017.

[15] Fattah, R., Chen, W., Wu, H., Wu, Y., and Zhang, X., "Noise Measurements of Generic Small-Scale Propellers," AIAA Paper 2019-2498, 2019.

[16] Brandt, J.B., "Small-Scale Propeller Performance at Low Speeds," M.S. Thesis, Department of Aerospace Engineering, University of Illinois at Urbana-Champaign, Urbana, IL, 2005.

[17] Deters, R.W., "Performance and Slipstream Characteristics of Small-Scale Propellers at Low Reynolds Numbers," Ph.D. Dissertation, Department of Aerospace Engineering, University of Illinois at Urbana-Champaign, Urbana, IL, 2014.

[18] MathWorks, "Periodogram power spectral density estimate," 2020. URL `https://www.mathworks.com/help/signal/ref/periodogram.html`.

[19] Tinney, C. E., and Sirohi, J., "Multirotor Drone Noise at Static Thrust," *AIAA Journal*, Vol. 56, No. 7, 2018, pp. 2816–2826. doi:10.2514/1.J056827.

[20] Stephenson, J. H., Tinney, C. E., Greenwood, E., and Watts, M. E., "Time frequency analysis of sound from a maneuvering rotorcraft," *Journal of Sound and Vibration*, Vol. 333, No. 21, 2014, pp. 5324–5339. doi:10.1016/J.JSV.2014.05.018.

[21] MathWorks, "Continuous Wavelet Transform and Scale-Based Analysis," 2020. URL `https://www.mathworks.com/help/wavelet/gs/continuous-wavelet-transform-and-scale-based-analysis.html`.

[22] Lilly, J. M., and Olhede, S. C., "On the analytic wavelet transform," *IEEE Transactions on Information Theory*, Vol. 56, No. 8, 2010, pp. 4135–4156. doi:10.1109/TIT.2010.2050935.

[23] MathWorks, "Continuous 1-D wavelet transform," 2020. URL https://www.mathworks.com/help/wavelet/ref/cwt.html.

[24] Lilly, J. M., and Olhede, S. C., "Higher-order properties of analytic wavelets," *IEEE Transactions on Signal Processing*, Vol. 57, No. 1, 2008, pp. 146–160. doi:10.1109/TSP.2008.2007607.

[25] MathWorks, "Morse Wavelets," 2020. URL https://www.mathworks.com/help/wavelet/ug/morse-wavelets.html.

[26] Hepperle, M., PropellerScanner, http://mh-aerotools.de, Accessed May 2, 2017.

[27] Uhlig, D. V., "Post Stall Propeller Behavior at Low Reynolds Numbers," M.S. Thesis, Department of Aerospace Engineering, University of Illinois at Urbana-Champaign, Urbana, IL, 2007.

[28] Uhlig, D. V. and Selig, M. S., "Post Stall Propeller Behavior at Low Reynolds Numbers," AIAA Paper 2008-0407, 2008.

[29] Yang, M., Darrah, D., Eppler, J., Liu, W., and Anemaat, W. A., "Small UAV Acoustic Design, Analysis and Testing," AIAA Paper 2019-1073, 2019.

[30] Henderson, B., and Huff, D., "Electric Motor Noise for Small Quadcopters: Part II-Source Characteristics and Predictions," AIAA Paper 2018-2953, 2018.

[31] Sinibaldi, G., and Marino, L., "Experimental analysis on the noise of propellers for small UAV," *Applied Acoustics*, Vol. 74, No. 1, 2013, pp. 79–88. doi:10.1016/j.apacoust.2012.06.011.